metals

MDPI

Article

Study on Reduction Melting Behavior of Iron-Bearing Burden Under Oxygen-Enriched Condition of Blast Furnace

Yuchen Zhang [1], Runsheng Xu [1,*], Jianliang Zhang [1], Rongrong Wang [2,3,*], Yongsheng Yang [1], Alberto N. Conejo [1] and Johannes Schenk [4]

[1] School of Metallurgical and Ecological Engineering, University of Science and Technology Beijing, Beijing 100083, China; yuchen19980629@163.com (Y.Z.); zhang.jianliang@hotmail.com (J.Z.); yangyongssheng@163.com (Y.Y.); aconejonava@hotmail.com (A.N.C.)
[2] Technical Support Center for Prevention and Control of Disastrous Accidents in Metal Smelting, University of Science and Technology Beijing, Beijing 100083, China
[3] Shunde Innovation School, University of Science and Technology Beijing, Foshan 528000, China
[4] Chair of Ferrous Metallurgy, Montanuniversitaet Leoben, Franz-Josef-Straβe 18, A-8700 Leoben, Austria; johannes.schenk@unileoben.ac.at
* Correspondence: xu_runsheng@163.com (R.X.); rongrong.wang@ustb.edu.cn (R.W.)

Abstract

The oxygen blast furnace (OBF) represents a key pathway toward deep decarbonization in ironmaking. The main difference between it and the traditional blast furnace is that the atmosphere in the furnace has high reduction potential and little nitrogen content. However, the burden metallurgical performance under CO-H_2-rich, N_2-lean atmospheres remains unclear. This study investigated the isothermal and non-isothermal reduction and softening–melting behavior of sinter and pellets. As CO increased from 59.2 to 79.2 vol%, the reduction degree rose from ~27% to ~90% within 180 min, with a rate index of 0.72–0.75%·min^{-1}. The apparent activation energies of sinter and pellets were 113.0 kJ·mol^{-1} and 57.9 kJ·mol^{-1}, respectively, indicating that the gas–solid interfacial chemical reaction is the rate-controlling step. Under non-isothermal conditions, the reduction start temperatures of both sinter and pellets decreased, and complete reduction was achieved at 1200 °C. Microstructural analysis revealed a four-stage structural evolution pathway. The softening–melting behavior indicated that oxygen-enriched conditions decrease the softening start temperature, whereas the melting start temperature increases due to the thickening of the metallic iron shell. The maximum pressure difference of the cohesive zone was reduced by 32.9%, and the air permeability was significantly improved. This study reveals the mechanism of charge reaction and structure evolution under OBF conditions and provides a theoretical basis for charge optimization and OBF operation control.

Keywords: oxygen blast furnace; iron-bearing burden; reduction behavior; softening–melting behavior

Check for updates

Academic Editor: Arne Mattias Thuvander

Received: 27 May 2026
Revised: 9 July 2026
Accepted: 10 July 2026
Published: 13 July 2026

Copyright: © 2026 by the authors. Licensee MDPI, Basel, Switzerland. This article is an open access article distributed under the terms and conditions of the Creative Commons Attribution (CC BY) license.

1. Introduction

The iron and steel industry is one of the most critical foundational material sectors worldwide. In 2025, global crude steel production exceeded 1.8 billion tons, approximately 70% of which was produced via the blast furnace–basic oxygen furnace (BF-BOF) route [1]. However, carbon emissions from blast furnace ironmaking account for more than 80% of the total emissions across the integrated process, and the steel industry contributes

approximately 7–9% of global CO_2 emissions [2,3]. Under the carbon neutrality target, the conventional blast furnace ironmaking route urgently requires transformation toward low- and ultimately zero-carbon pathways [4].

Currently, low-carbon ironmaking technologies primarily encompass pathways such as hydrogen-rich blast furnace injection, gas-based shaft furnace direct reduction (DRI), smelting reduction, and molten salt electrolysis. Hydrogen-rich injection in blast furnaces reduces the coke ratio by increasing the proportion of H_2-based reduction within the furnace; while this approach offers the advantage of good compatibility with existing blast furnace processes, its carbon reduction potential is relatively limited due to constraints imposed by the furnace's thermal balance [5,6]. Gas-based shaft furnace direct reduction is exemplified by the Midrex and Tenova Energiron processes. Utilizing hydrogen-rich gas to reduce iron ore offers significant emissions reduction potential when supplied with green hydrogen, though the process relies heavily on high-grade pellets and low-cost green hydrogen resources. Smelting reduction processes (such as FINEX) can directly utilize non-coking coal and iron ore fines and involve a shorter process flow; however, issues such as high energy consumption and limited refractory service life persist [7]. Molten salt electrolysis for ironmaking is considered a key direction for future near-zero-carbon iron production, though it currently remains in the laboratory and pilot-scale research stage [8]. In contrast, the oxygen blast furnace (OBF) offers both carbon reduction potential and engineering feasibility. This process utilizes high-purity oxygen instead of the traditional hot blast and reinjects decarbonized top gas into the furnace; this significantly increases the concentrations of CO and H_2 within the furnace while eliminating the unproductive heat load associated with nitrogen, thereby achieving a CO_2 reduction of approximately 24% to 26%. More importantly, OBF technology can fully utilize existing blast furnace equipment and raw material systems; it is particularly well-suited to my country's iron and steel industry, which relies primarily on sinter and conventional pellets as furnace feed, and is therefore considered one of the low-carbon blast furnace technologies with the greatest potential for industrialization at this stage [9]. Against this backdrop, conducting in-depth research into the reduction, softening, and melting behaviors of furnace burden under conditions of high reduction potential and high hydrogen-rich recycled gas in an oxygen-enriched blast furnace holds significant theoretical importance for optimizing burden structure, improving burden column permeability, and advancing the industrial application of oxygen-enriched blast furnace technology.

At present, frontier low-carbon ironmaking routes primarily include hydrogen-based direct reduction [10,11], smelting reduction [12], electrolysis-based ironmaking [13], and the oxygen blast furnace (OBF). Among these, the oxygen blast furnace (OBF) employs oxygen in place of preheated air for tuyere injection and recycles purified top gas as an auxiliary reductant. This fundamentally eliminates the "invalid heat consumption" carried by a large amount of N_2, greatly increases the partial pressure of CO and H_2 in the furnace, and creates conditions for the enrichment and capture of blast furnace gas [14,15]. The European ULCOS project and multiple industrial trials in Asia have demonstrated that, without altering the core blast furnace configuration, the OBF process can reduce CO_2 emissions by 24–26%, indicating strong near-term potential for industrial deployment [16,17]. From the perspective of metallurgical thermodynamics and kinetics, the operation of OBF has a global impact on the furnace internal environment. Compared with the top gas composition in a conventional blast furnace, the oxygen blast furnace exhibits CO concentrations of 60–80 vol% and H_2 levels of approximately 10–20 vol%, while the N_2 content is nearly negligible [18,19]. This strongly reducing atmosphere directly influences the reduction behavior of iron-bearing burden materials and the position and thickness of the soft melting zone, as well as the distribution and permeability of the internal gas flow [20,21].

Under conventional blast furnace conditions, the reduction kinetics of iron-bearing burden materials have been extensively investigated, elucidating the stepwise reduction pathways of iron oxides and identifying gas–solid interfacial chemical reaction or mixed internal diffusion as the predominant rate-controlling mechanisms [22–24]. Studies have shown that H_2, owing to its smaller kinetic molecular diameter and higher mutual diffusivity, exhibits superior reduction capability in the low-temperature regime and can synergistically promote CO reduction via the water–gas shift reaction [25,26]. However, most existing kinetic datasets are based on simplified binary gas atmospheres (CO/CO_2 or H_2/H_2O), which fail to faithfully reproduce the CO-CO_2-H_2 ternary gas environment characteristic of the OBF. Moreover, quantitative kinetic studies on industrial-grade sinter and pellets under OBF-relevant temperature ranges and multi-component gas gradients remain relatively limited [27].

The softening–melting behavior is a key metric for evaluating the metallurgical performance of iron-bearing burden materials in the blast furnace, which directly determines the position and thickness of the cohesive zone, as well as its permeability, thereby influencing gas flow distribution and thermal efficiency [28]. Previous studies have shown that under conventional blast furnace conditions, increasing the reduction degree of the burden prior to charging decreases softening start temperature (T_{10}), while pressure difference (ΔP_{max}) is primarily governed by slag viscosity [29]. Under OBF conditions, the significantly elevated pre-reduction degree and variations in slag composition are expected to systematically influence softening–melting parameters, while systematic investigations under OBF-specific gas atmospheres and heating regimes remain limited [30].

In summary, previous studies have predominantly focused on simplified single-component gas atmospheres and have treated reduction kinetics and high-temperature deformation behavior as separate subjects. To address this limitation, the present study draws on actual operating parameters from 1000 m^3 and 2000 m^3 oxygen blast furnaces (OBF) and a one-dimensional axial heat balance model to construct the full-furnace temperature–gas distribution field. Systematic isothermal and non-isothermal reduction experiments, together with high-temperature softening–melting tests, were then conducted to elucidate the full-lifecycle reaction and deformation behavior of burden materials under the authentic thermal conditions of low-carbon oxygen blast furnaces. A three-tier progressive approach was adopted. First, the coupled process between thermodynamic conditions and multi-component gas (CO-CO_2-H_2) gradients during burden descent was precisely reconstructed, based on the operational characteristics of industrial-scale blast furnaces and the one-dimensional axial heat balance model. Second, isothermal and non-isothermal reduction kinetic analysis, high-temperature softening–melting experiments, and SEM/EDS microstructural characterization were combined to systematically decouple the full reaction chain connecting reduction kinetics, microstructural evolution, and gas–liquid permeability rheology. This revealed the reduction behavior, kinetic mechanisms, and phase transformation of sinter and pellets under multi-component gas and variable-temperature conditions. The core innovations are embodied in the revelation of two key mechanisms. The first is the differential evolution of micro-mineral phases governed by multi-component gas–solid interfacial reactions. The second is how, under non-isothermal conditions with high-reduction-potential gas, the structural support effect of the metallic iron shell effectively counteracts slag–liquid infiltration, thereby reducing the cohesive zone pressure drop by 32.9%. These findings provide a comprehensive theoretical foundation for burden optimization and gas permeability control in low-carbon oxygen blast furnaces.

2. Materials and Methods

2.1. Materials

The industrial sinter and pellets used in this study were obtained from a large-scale iron and steel enterprise in China, and their detailed chemical compositions are listed in Table 1. TFe and FeO were determined according to GB/T 6730.5 and GB/T 6730.8, respectively, whereas the major gangue constituents, including SiO_2, CaO, MgO, and Al_2O_3, were analyzed in accordance with GB/T 6730.62 [31–33]. According to the relevant Chinese national standards, the absolute errors for TFe and FeO do not exceed ±0.20% and ±0.15%, respectively; the errors for the major gangue components are within ±0.15%, and those for trace components are within ±0.08%.

Table 1. Chemical composition of sinter and pellets, wt%.

	TFe	Fe_2O_3	FeO	SiO_2	CaO	MgO	Al_2O_3
Sinter	55.52%	68.61%	8.56%	6.03%	11.16%	1.46%	1.17%
Pellets	63.20%	85.86%	3.54%	4.85%	1.02%	0.58%	1.43%

Here, total iron content (TFe) refers to the total mass percentage of iron present in all forms in the iron-bearing burden materials. From the perspective of elemental mass conservation, the measured TFe, Fe_2O_3, and FeO contents listed in Table 1 show good internal consistency. Stoichiometric conversion indicates that Fe_2O_3 (68.61%) and FeO (8.56%) in the sinter contribute an equivalent total iron content of 54.64%, which is in close agreement with the directly measured TFe value of 55.52%. For the pellets, the calculated equivalent total iron content is 62.80%, with an absolute deviation of only 0.40% from the measured TFe value of 63.20%.

With respect to gangue composition, the sinter is characterized by a high CaO content (11.16%) and high binary basicity (CaO/SiO_2 = 1.85), corresponding to a typical high-basicity self-fluxing sinter. In contrast, the pellets exhibit a relatively high SiO_2 content (4.85%) and low basicity, thereby showing pronounced acidic characteristics. This asymmetric burden configuration, namely "high-basicity sinter + acidic pellets," provides an important material basis for the subsequent investigation of high-temperature softening–melting interactions, cohesive-zone formation behavior, and gas permeability optimization in the blast furnace. To ensure consistent boundary conditions for the reduction kinetics and high-temperature deformation tests, the particle size of both raw materials was strictly controlled within the range of 10.0–12.5 mm.

2.2. Isothermal Reduction Experiment

The isothermal reduction experiments were conducted using a programmable reduction furnace independently developed by the University of Science and Technology Beijing, as shown in Figure 1. The apparatus consists of a control system, a gas supply system, a heating furnace, and a high-precision electronic balance. It enables precise control of the heating profile and furnace atmosphere according to predefined programs, while continuously recording the mass change of the sample in real time via the electronic balance.

Experimental conditions were based on GB/T 13241-2017, and gas compositions were adjusted according to the actual operating conditions of an oxygen blast furnace [34]. From 200 to 900 °C, N_2 was introduced as a protective gas at a flow rate of 5 $L \cdot min^{-1}$. Upon reaching 900 °C, the N_2 flow rate was increased to 15 $L \cdot min^{-1}$ and maintained for 30 min. Subsequently, the gas was switched to reducing gas at 15 $L \cdot min^{-1}$, and isothermal reduction was conducted for 180 min. The gas compositions employed for isothermal

reduction are listed in Table 2, comprising three atmospheres with progressively increasing reducing potential.

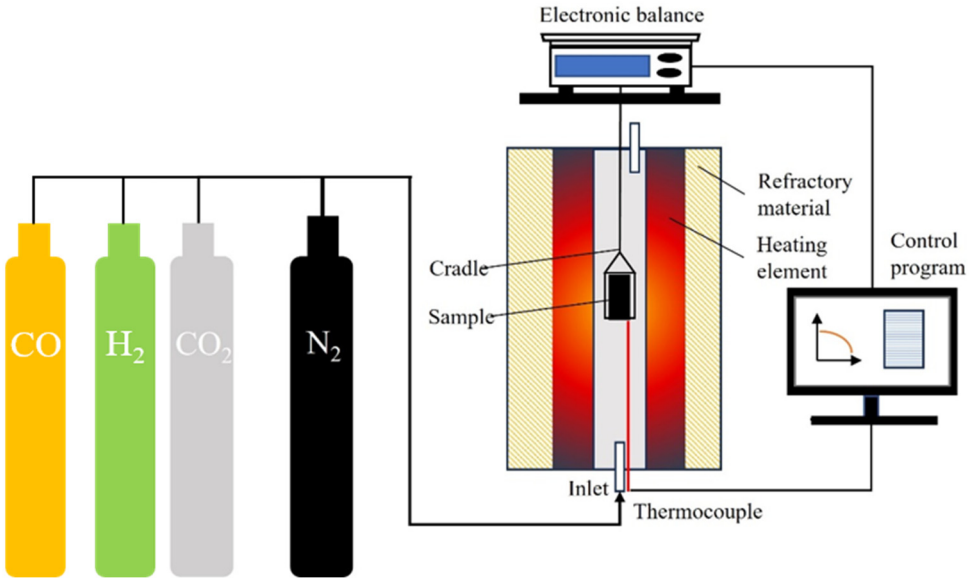


Figure 1. Programmable reduction furnace.

Table 2. Reducing gas ratio.

Number	Reduction Atmosphere
1	59.2%CO + 30%CO_2 + 10%H_2 + 0.8%N_2
2	69.2%CO + 20%CO_2 + 10%H_2 + 0.8%N_2
3	79.2%CO + 10%CO_2 + 10%H_2 + 0.8%N_2

During the reduction process, the temperature of the inlet gas and that of the entire sample bed were maintained at 900 ± 5 °C. Upon completion of the reduction, the reducing gas was shut off and N_2 was immediately introduced at 15 L·min^{-1} to purge the residual reducing gas from the pipeline and the reaction tube.

The reduction degree R_t is calculated according to Equation (1):

$$R_t(\%) = \left(\frac{0.111W_1}{0.430W_2} + \frac{m_1 - m_t}{m_0 \times 0.430W_2} \times 100\right) \times 100 \quad (1)$$

where m_0 is the mass of the sample (g); m_1 is the total mass of the sample and the reduction apparatus before reduction (g); m_t is the total mass of the sample and the reduction apparatus after reduction for time t minutes (g); W_1 is the ferrous iron content in the sample before reduction, expressed as a mass fraction (%); and W_2 is the total iron content in the sample before reduction, expressed as a mass fraction (%).

The corresponding time when the reduction degree reaches 30% and 60% is read from the reduction curve, and the unit is minute (min). The reduction rate index (RVI) was calculated according to Equation (2):

$$\mathrm{RVI} = \mathrm{d}R_t/\mathrm{d}t = 33.6/(t_{60} - t_{30}) \quad (2)$$

where t_{30} is the time required to reach a reduction degree of 30% (min), and t_{60} is the time required to reach a reduction degree of 60% (min).

To ensure the reliability and statistical representativeness of the core kinetic parameters, including the reduction degree (Rt) and the reduction velocity index (RVI), we conducted

multiple batches of in situ parallel reproducibility tests for both isothermal and non-isothermal gas–solid reactions of the two burden materials under identical temperature and multi-component gas atmosphere conditions. With precise regulation of the ternary gas flow by four parallel mass flow controllers and second-level online mass acquisition by the suspended high-sensitivity electronic balance, the experimental system effectively eliminated disturbances caused by unsteady gas flow fluctuations. Statistical error analysis shows that the absolute standard deviation of the dynamic reduction degree for both sinter and pellets along the entire continuous time axis is strictly within ±1.2%, demonstrating good reproducibility.

2.3. Non-Isothermal Reduction Experiment

The core objective of the non-isothermal reduction experiments is to achieve high-fidelity reproduction of the continuous variable-temperature thermal flux and dynamic gas concentration gradients experienced by the composite burden during its descent through the blast furnace lumpy zone. To this end, a process-analysis mathematical model was first constructed, based on the closure of real oxygen blast furnace mass and energy flows [35,36]. The model uses field-measured core parameters from 1000 m^3 and 2000 m^3 oxygen blast furnaces: the 1000 m^3 furnace has a daily iron output of 4500 t/d, a coke ratio of 282 kg/t, an ore consumption of 1664 kg/t, and an effective volume of 1212 m^3. The 2000 m^3 furnace has a daily iron output of 7000 t/d, with all other parameters identical. By calculating the raw material volume per ton of iron and accounting for a 10% column compression ratio, the total smelting times were determined to be 4.83 h and 7.14 h for the two furnaces, respectively. A descent velocity formula was further applied to compute the downward speed at each key position, yielding values of 9.87 m/h for the 1000 m^3 furnace and 7.83 m/h for the 2000 m^3 furnace. The residence time in each zone was then derived, giving total burden running times of 4.3 h and 6.37 h, respectively. Finally, by coupling the numerical simulation results of the axial multi-component gas flow inside the furnace, the spatial displacement was mapped onto the time control steps of the laboratory tube furnace.

For the 1000 m^3 furnace, the total residence time is 180 min, with the following heating program: room temperature → 200 °C (15 min, 12 °C/min) → 1000 °C (135 min, 6 °C/min) → 1250 °C (30 min, 8.3 °C/min). For the 2000 m^3 furnace, the total residence time is 260 min, with the heating program adjusted to the following: room temperature → 200 °C (15 min, 12 °C/min) → 1000 °C (210 min, 3.8 °C/min) → 1250 °C (35 min, 7.1 °C/min). This dynamic parameter deployment, grounded in industrial big data, ensures that the heating strategy accurately reproduces the real non-isothermal thermal trajectory inside the furnace. It thus provides a reliable methodological basis for analyzing the deformation behavior of burden materials under the strongly reducing atmosphere of oxygen blast furnaces.

On this basis, combined with numerical simulation results of the temperature and atmosphere in oxygen blast furnaces reported in the literature, as well as the residence time of the burden in different furnace zones, the heating rates and reducing gas compositions for each temperature interval were determined [37,38]. Accordingly, a non-isothermal reduction experimental scheme representative of actual operating conditions was established, as shown in Figure 2. A standard heating schedule and gas atmosphere specified by national standards were adopted as the reference benchmark, and interrupted sampling was conducted at 350 °C, 700 °C, 1000 °C, and 1200 °C to characterize the microstructural and phase evolution at different stages of reduction.

The samples after reduction at different temperatures were cold-inlaid to prepare metallographic polished sections, and the microstructure and phase distribution were characterized by scanning electron microscopy.

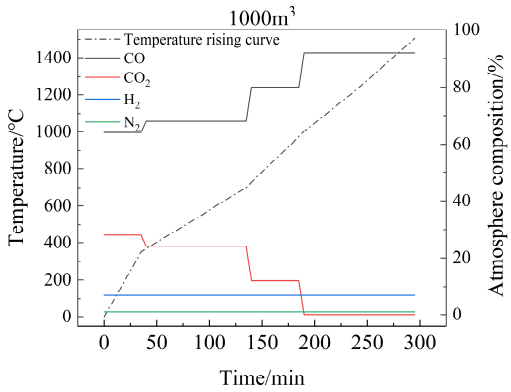


Figure 2. Heating system and atmosphere under oxygen blast furnace conditions.

2.4. Softening–Melting Experiment

Based on the burden distribution of the steel plant (70% sinter + 30% pellets), the iron-bearing charge was configured with 350 g of sinter and 150 g of pellets, together with 120 g of coke (80 g placed in the lower crucible layer and 40 g distributed above the iron-bearing burden). The particle sizes of both the iron-bearing materials and coke were controlled within 10–12.5 mm. Figure 3 shows the dynamic heating program and the gradient change process of the multi-component gas atmosphere in the load softening experiment, which is used to simulate the thermal conditions and low-carbon reducing atmosphere experienced by the iron-containing furnace charge during the blast furnace descent. The traditional operating condition program is based on the standard GB/T 34211-2017 [39]; the operating condition programs for 1000 m^3 and 2000 m^3 all-oxygen blast furnaces are based on the mathematical model of the smelting cycle described in Section 2.3 and the results of the one-dimensional blast furnace axial thermal balance simulation. Specifically, the descent rate of the furnace charge, the heat conduction characteristics, and the axial distribution of gas components in blast furnaces of different volumes are transformed into temperature control curves and gas flow regulation schemes in load experiments. The dashed line in the figure represents the non-isothermal heating trajectory of the sample layer, and the solid lines of different colors represent the stepwise changes in the volume fractions of gases such as CO, CO_2, H_2 and N_2 with reaction time. Through this spatiotemporal transformation method, the experiment can effectively simulate the process of the composite furnace charge gradually descending from the upper blocky zone and softening and melting into the softening zone under real OBF strong reduction and high hydrogen-rich gas conditions. This provides reliable physical simulation conditions for determining key metallurgical performance indicators such as the initial softening temperature T_{10}, the final softening temperature T_{40}, the initial melting temperature T_s, the dripping temperature T_d, and the maximum pressure difference ΔPmax of the bonding zone.

In addition, multiple rounds of parallel calibration and regression tests were performed on the load-bearing reaction and deformation process of the burden bed. The results indicate that the characteristic softening start temperature (T_{10}) and softening end temperature (T_{40}), automatically recorded by the displacement sensors, exhibit an absolute reproducibility deviation stable within ±4 °C. The fluctuation tolerance of the melting start temperature (T_s) and dripping temperature (T_d), captured in real time by the differential pressure transmitter, is strictly controlled within ±5 °C. Meanwhile, the absolute standard deviation of the parallel measurements of the maximum pressure drop (ΔPmax) converges within ±25 Pa. To avoid visual conflict between discrete error bars and densely arranged multi-component bar charts, we chose not to superimpose error bars on the figures. Instead, we provide the above methodological clarification to support a clear and reliable data

foundation for the theoretical reconstruction of the permeability barrier in low-carbon oxygen blast furnaces.

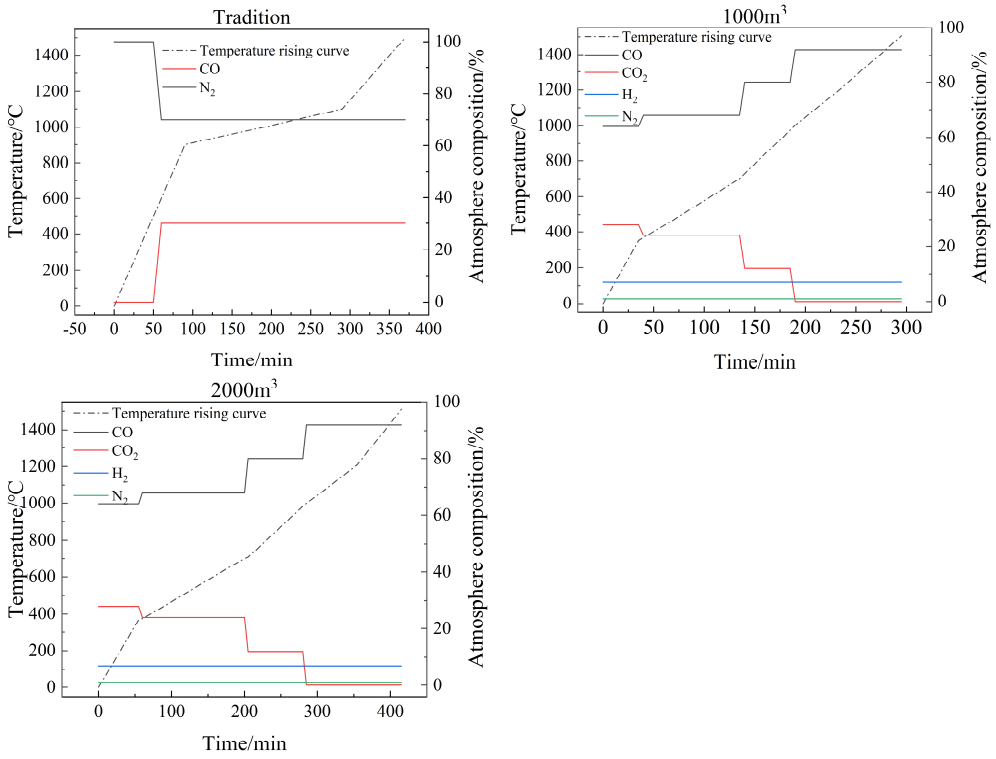
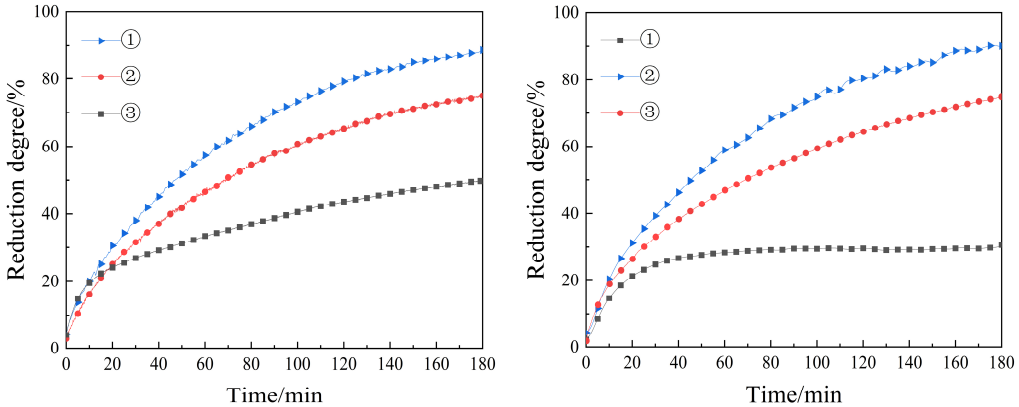


Figure 3. Temperature rise and atmosphere change in softening–melting experiment.

3. Results

3.1. Isothermal Reduction Behavior of Iron-Bearing Burden

Figure 4 presents the Reduction degree vs. Time curves of sinter and pellets under different reducing atmospheres. Table 3 summarizes the R_t and the RVI for each condition. Overall, for both sinter and pellets, the reduction curves shift progressively to the left with increasing CO concentration in the atmosphere, indicating that higher reduction degrees are achieved within the same duration and that the reduction rate is markedly accelerated.



(**a**) Sinter (**b**) Pellets

Figure 4. Reduction degree of sinter pellets under different reducing atmosphere conditions.

Table 3. Reduction degree and reduction rate of burden under different reduction atmosphere conditions.

	Furnace Atmosphere	Rt	RVI/(%/min)
Sinter	① 59.2%CO + 30%CO_2 + 10%H_2 + 0.8%N_2	26.86%	/
	② 69.2%CO + 20% CO_2 + 10%H_2 + 0.8%N_2	74.98%	0.471
	③ 79.2%CO + 10% CO_2 + 10%H_2 + 0.8%N_2	88.67%	0.722
Pellets	① 59.2%CO + 30% CO_2 + 10%H_2 + 0.8%N_2	30.58%	/
	② 69.2%CO + 20% CO_2 + 10%H_2 + 0.8%N_2	74.69%	0.433
	③ 79.2%CO + 10% CO_2 + 10%H_2 + 0.8%N_2	90.25%	0.748

At the lowest CO concentration, the reduction degree of sinter reached only 26.86% after reduction for 180 min, and the reduction rate was too low to allow calculation of the RVI. When the CO concentration increased to 69.2% (②), the R_t rose to 74.98%, with an RVI of 0.471%·min^{-1}. Further increasing the CO concentration to 79.2% (③) resulted in a reduction degree of 88.67%, accompanied by a marked increase in RVI to 0.722%·min^{-1}. Pellets exhibit a trend similar to that of sinter. As the CO concentration increases from 59.2% to 79.2%, the RVI of pellets rises from 0.433%·min^{-1} to 0.748%·min^{-1}, while the final reduction degree increases from 30.58% to 90.25%. This behavior is primarily attributed to the dominant reactions between CO and iron-bearing burden materials at around 1000 °C, as follows:

$$3Fe_2O_3 + CO \rightarrow 2Fe_3O_4 + CO_2 \quad (3)$$

$$Fe_3O_4 + CO \rightarrow 3FeO + CO_2 \quad (4)$$

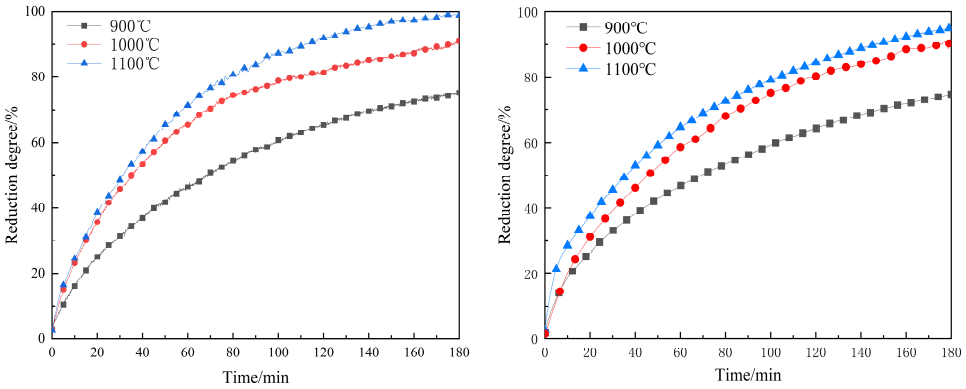
$$FeO + CO \rightarrow Fe + CO_2 \quad (5)$$

An increase in the CO concentration directly elevates its partial pressure, shifting the reduction equilibria toward the products and thereby improving the thermodynamic conditions, which promotes the stepwise reduction of iron oxides to metallic iron.

Figure 5 shows the Reduction degree vs. Time curves of sinter and pellets at different reduction temperatures. Table 4 summarizes the final reduction degree (R_t) and the reduction rate index (RVI) at each temperature. The experimental results show that temperature is the key thermodynamic parameter affecting the reduction kinetics of furnace burden. With the increase in temperature from 900 °C to 1100 °C, the reduction reaction of sinter and pellets increased significantly. The final reduction degree of sinter increased from 74.98% to 98.92%, and the RVI increased from 0.472%/min to 1.163%/min. The final reduction degree of pellets also increased from 74.69% to 95.18%. At 900 °C, the RVI values of the two types of burden are comparable, with a difference of approximately 8.9%, indicating that their reduction kinetic characteristics are similar at lower temperatures. As the temperature rises to 1100 °C, the difference widens to about 37.7%, indicating that high temperature has a more significant effect on the reduction rate of sinter.

Table 4. Reduction degree and reduction rate of sinter pellets at different temperatures.

	Temperature	Rt	RVI/(%/min)
Sinter	900 °C	74.98%	0.472
	1000 °C	90.93%	0.973
	1100 °C	98.92%	1.163
Pellets	900 °C	74.69%	0.433
	1000 °C	90.25%	0.748
	1100 °C	95.18%	0.844



(**a**) Sinter (**b**) Pellets

Figure 5. Reduction degree of sinter and pellets at different temperatures.

This is because the sinter has more open pores, which is conducive to the infiltration of reducing gas into the interior; the structure of pellets is relatively dense, and the internal diffusion resistance is relatively large. The improvement effect of high temperature conditions on its kinetics is restricted to a certain extent. As far as the final reduction degree is concerned, the sinter is obviously better than the pellets at 1100 °C, but both are about 74.7% at 900 °C, indicating that the low temperature conditions have obvious limitations on the final reduction degree of the two kinds of burden.

The enhancement in reduction behavior with increasing temperature is governed by the combined effects of thermodynamics and kinetics. On the one hand, as shown in Figure 6, the reduction of FeO to metallic iron is a mildly exothermic reaction, and elevated temperatures to some extent limit the equilibrium conversion in the forward direction. On the other hand, elevated temperatures markedly improve the diffusion kinetics of the reducing gases and exponentially increase the rate constant of the gas–solid interfacial reaction. This kinetic advantage far outweighs the minor shift in thermodynamic equilibrium, resulting in a pronounced increase in the overall apparent reduction rate with temperature.

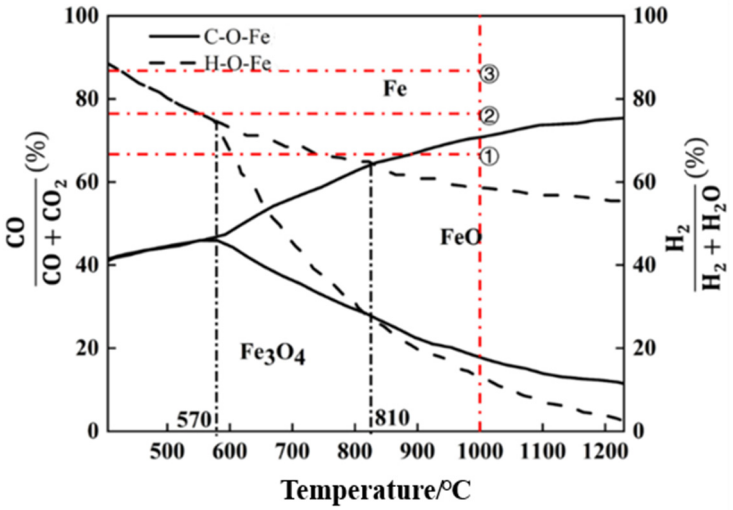


Figure 6. The relationship between iron, iron oxides and CO-CO_2, H_2-H_2O gas equilibrium.

3.2. Isothermal Reduction Kinetics

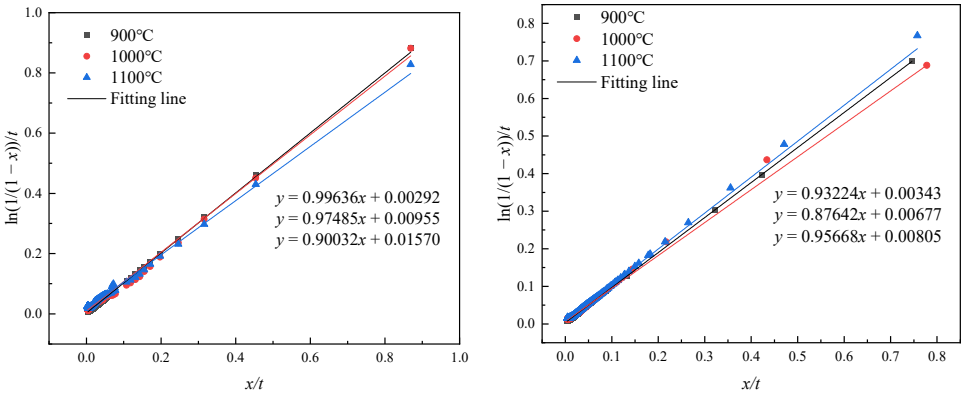
As the reduction-time curve clearly shows, as the reduction reaction continues, due to the continuous thickening of the newly formed outer metallic iron shell and high-temperature micro-sintering, the escape of gaseous reduction products and the surge in internal diffusion resistance of the reducing gas cause the overall reaction rate to gradually

decrease and eventually stabilize with the extension of reduction time. This phenomenon, characterized by an extremely high kinetic rate in the initial stage of the reaction followed by a rapid and precipitous drop, reflects typical high-temperature gas–solid reduction self-resistance behavior. In view of this, in order to accurately quantify this spatiotemporal resistance that dynamically evolves with the increase in reactant conversion rate in the mathematical model, this study introduces the Drozdzov equation (Equation (6)) with self-resistance coefficient, which is widely used in the classical gas–solid reaction kinetics theory, to analyze this unsteady reduction kinetic process. The model and its related methodological calculation strategies have been widely verified and applied in the classical kinetic literature on blast furnace raw materials, such as Heikkinen [23] et al. on the modeling of pellet reduction kinetics under blast furnace atmosphere and Cao [24] et al. on the non-isothermal reduction characteristics and kinetic analysis of hematite under hydrogen-rich atmosphere. By introducing this equation, the complex nonlinear gas–solid conversion process can be reconstructed into an excellent linear kinetic relationship, thus laying a solid methodological foundation for the high-reliability extraction of the apparent activation energy under the gas–solid interface reaction control step using the Arrhenius relation.

$$\frac{1}{t}\ln\frac{1}{1-x}-\beta\frac{x}{t}=K_m \tag{6}$$

where t is the reaction time, min; x is the reduction degree, %/%; β is the self-resistance coefficient; and K_m is the reaction rate constant, min^{-1}.

According to the Drozdzov equation, a linear relationship exists between the relevant transformation variables, in which the slope of the fitted line corresponds to the self-resistance coefficient and the intercept represents the rate constant of the reduction reaction. Based on the experimental data, scatter plots were constructed and linearly fitted to obtain the corresponding relationships, as shown in Figure 7.



(**a**) Sinter (**b**) Pellets

Figure 7. Linearly fitting curves of $\frac{1}{t}\ln\frac{1}{1-x}$ and $\frac{x}{t}$.

With the obtained reaction rate constant, the apparent activation energy of the reduction reaction can be obtained by linear fitting of $\ln K_m$ and T^{-1} using the Arrhenius equation.

$$\ln K_\mathrm{m}=\ln A-\frac{E_\mathrm{a}}{RT} \tag{7}$$

where K_m is the reaction rate constant; A is the frequency factor; E_a is the apparent activation energy, J/mol; R is the gas constant, 8.314J/mol; and T is reduction temperature, K. According to the fitting results in Table 5, the reaction rate constants (K_m) for both sinter and pellets exhibit a clear positive correlation with temperature, with R^2 exceeding 90%, indicating that the Drozdzov model provides a satisfactory description of the process.

Table 5. Fitted data.

	Temperature	K_m	β	R^2
Sinter	900 °C	0.00292	0.99636	0.9981
	1000 °C	0.00955	0.97485	0.9936
	1100 °C	0.01570	0.90032	0.9649
Pellets	900 °C	0.00343	0.93224	0.9999
	1000 °C	0.00677	0.87642	0.9843
	1100 °C	0.00805	0.95668	0.9888

The relationship curve between the reduction degree $\ln K_m$ and T^{-1} is shown in Figure 8. The fitting degree R^2 of the sintering curve is 0.9173, and the fitting degree R^2 of the pellets curve is 0.9209. According to the calculation, the apparent activation energy of the sinter reduction reaction is 113 kJ·mol^{-1}. The apparent activation energy of the pellets reduction reaction is 57.898 kJ·mol^{-1}. In general, the activation energy for diffusion-controlled processes is less than 13 kJ·mol^{-1}, whereas that for interfacial chemical reaction-controlled processes is typically greater than 40 kJ·mol^{-1}; mixed control mechanisms generally exhibit activation energies in the range of 20–35 kJ·mol^{-1}. The apparent activation energies for the reduction of both sinter and pellets are significantly greater than 40 kJ·mol^{-1}, indicating that their reduction processes are predominantly controlled by the gas–solid interfacial chemical reaction step.

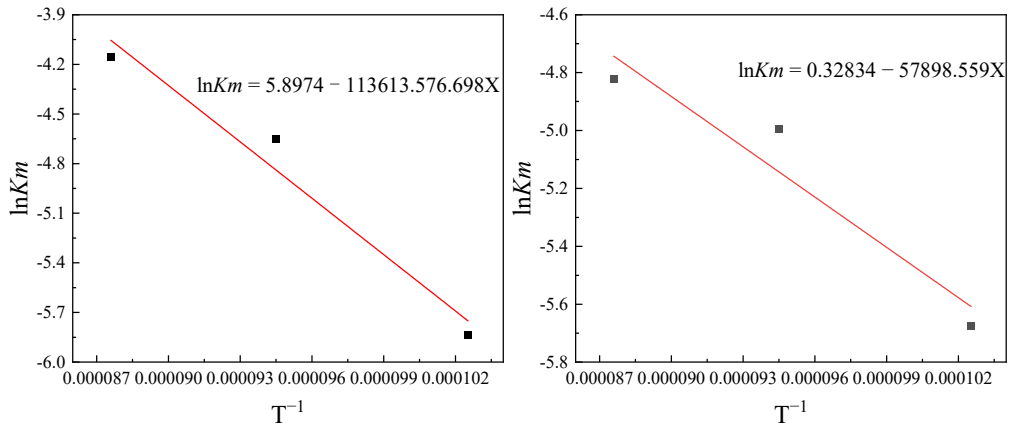


Figure 8. Relationship between $\ln K_m$ and T^{-1}.

Although the solid-state reduction of both sinter and pellets is governed by gas–solid interfacial chemical reactions, their apparent activation energies exhibit a notable divergence. This behavior is highly consistent with existing reports on the evolution of kinetic energy barriers for iron oxide reduction under hydrogen-rich blast furnace atmospheres [27]. The microstructure of sinter is highly heterogeneous and contains substantial amounts of silicate glass matrix and acicular calcium ferrite bonding phases. These stable solid-phase encapsulants tightly interlock the iron oxide grains, imposing considerable structural resistance to interfacial gas adsorption and oxygen removal, resulting in a systematically higher apparent activation energy. In contrast, pellets are composed of uniformly arranged high-purity hematite grains. During the early stages of non-isothermal reduction, the anisotropic lattice expansion associated with the Fe_2O_3 to Fe_3O_4 transformation readily generates dense microcrack networks within the particles. These newly formed defects facilitate inward gas permeation and expose a large number of unreacted, highly active interfaces. This mechanism is consistent with the aforementioned kinetic derivation and with recent reports on crack-related effects during hematite reduction under low-carbon, hydrogen-

rich, variable-temperature conditions, providing a microstructure-based explanation for the significantly lower apparent activation energy of pellets.

3.3. Non-Isothermal Reduction Behavior and Microstructure Evolution of Iron-Bearing Burden

Figure 9 shows the reduction curves of sinter at different temperatures. At temperatures below 350 °C, the samples exhibit negligible mass change; this stage primarily corresponds to the release of crystallization water and a small amount of volatile matter. The reduction degree of sinter reaches 28.82% at 700 °C, 86.66% at 1000 °C, and 99.89% at the end point of 1200 °C. The oxygen-enriched blast furnace process markedly increases the concentrations of CO and H_2 in the gas phase, thereby significantly lowering the reduction onset temperature of iron-bearing burden materials and enabling higher reduction degrees to be achieved at lower temperatures.

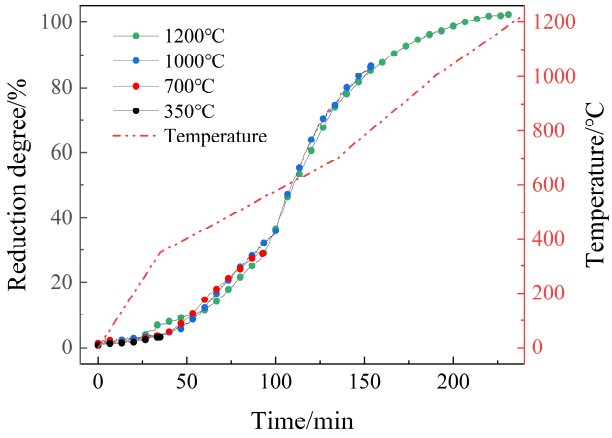


Figure 9. Reduction curves of sinter at different temperatures.

The trend of the non-isothermal reduction curve of pellets is similar to that of sinter. However, a notable difference is observed. Pellets show an obvious weight loss stage at about 40 min, as shown in Figure 10. This behavior can be attributed to two main factors. First, the markedly increased H_2 concentration in the atmosphere enhances the reducing potential at low temperatures; owing to its smaller molecular size and higher mutual diffusivity, H_2 exhibits superior reduction capability in this regime. Second, the iron oxides in pellets are predominantly in the form of hematite, and their higher oxidation state enables rapid reduction to FeO by H_2 at relatively low temperatures, leading to a pronounced mass loss in the low-temperature range.

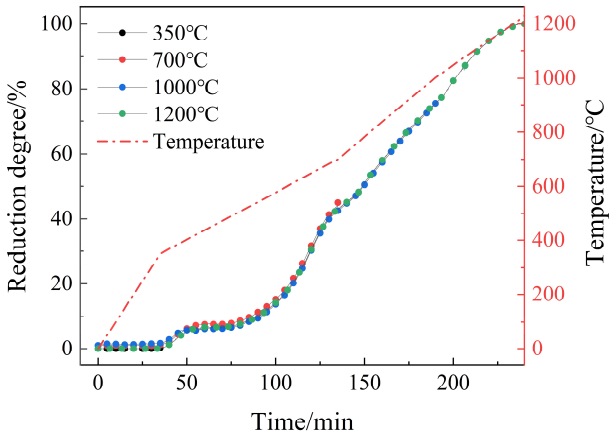


Figure 10. Reduction curves of pellets at different temperatures.

From a thermodynamic perspective, when the temperature exceeds 810 °C, the reducing ability of H_2 toward iron oxides becomes stronger than that of CO. From a kinetic standpoint, the smaller molecular size and higher diffusivity of H_2 confer a faster gas-phase mass transfer rate. In addition, the presence of the water-gas shift reaction enables H_2 to synergistically promote CO reduction; moreover, when the temperature exceeds 800 °C, the reduction rate of CO becomes extremely rapid. The introduction of H_2 significantly improved the reduction kinetic conditions of iron-bearing burden.

The microstructure of sinter after reduction at different temperatures was analyzed, as shown in Figure 11. At 350 °C, the iron-containing phase in the sinter is still dominated by Fe_3O_4, and no obvious reduction has occurred; at 700 °C, Fe_2O_3, Fe_3O_4 and wustite can be observed at the same time, indicating that part of Fe_2O_3 has been reduced to Fe_3O_4 and wustite, but no metallic iron has formed. At 1000 °C, wustite is extensively reduced to metallic iron, which appears as dispersed, fragment-like particles distributed within the original iron oxide regions. Calcium ferrites are further reduced to form metallic iron and calcium silicates. The formation of a limited peripheral sintered layer partially impedes the contact between internal wüstite and the reducing gases; at 1200 °C, the original iron oxide regions are completely reduced to lamellar metallic iron. The calcium ferrite regions transform into lath-like calcium silicates, with metallic iron aggregating along the boundaries of the silicate phase, resulting in well-defined microstructural features.

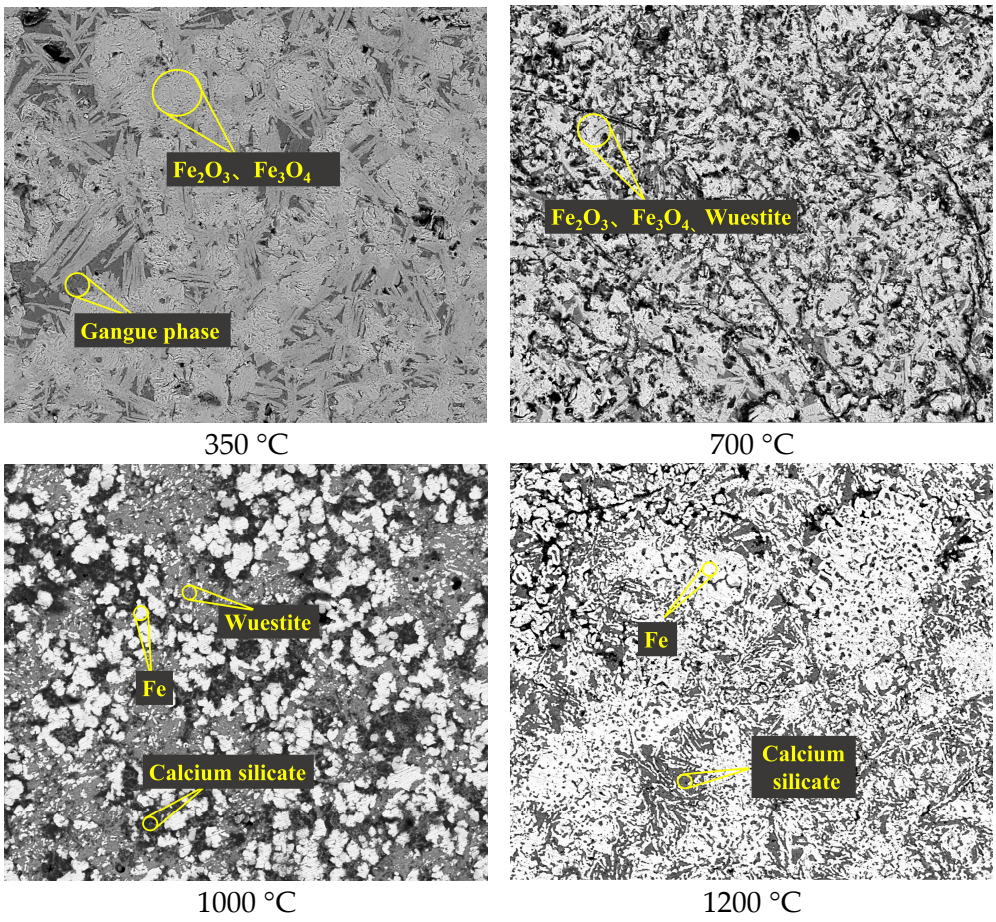


Figure 11. Microscopic morphology of sinter in different reduction stages.

The microstructure evolution path of pellets is similar to that of sinter, but there are also differences, as shown in Figure 12. At 350 °C, there is almost no reduction of pellets, and the particles are mainly hematite with a clear boundary; gangue minerals are distributed in the form of silicate. At 700 °C, hematite is partially reduced to magnetite, and then a small

amount of wustite is formed; cracks caused by reduction expansion can be seen inside the particles, but there is almost no metal iron formation. At 1000 °C, the reduction reaction is intense, a large amount of wustite is transformed into metallic iron, which is dispersedly distributed, and a small island-like aggregation area is formed between adjacent particles. The formed metallic iron layer has a hindered effect on the contact between the internal wustite and the reducing gas. At 1200 °C, most of the iron oxides are completely reduced, the metallic iron aggregates, merges and grows to form large metallic iron particles, and the connectivity is enhanced.

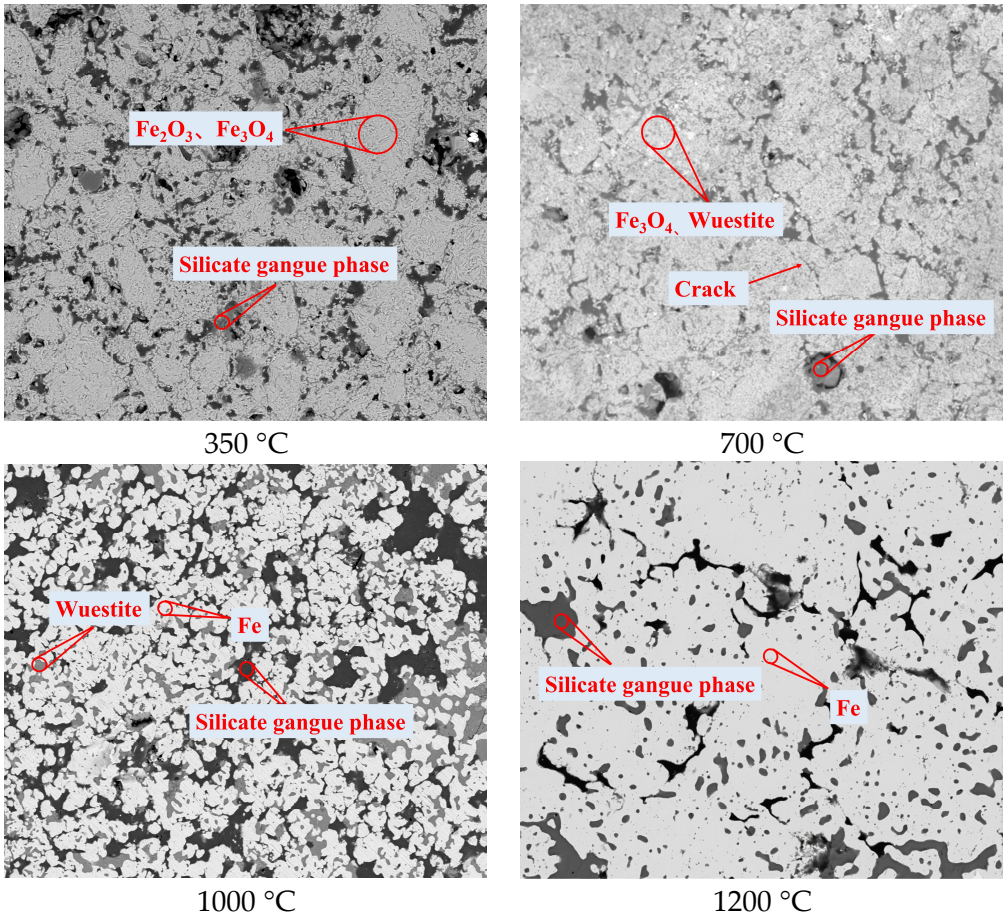


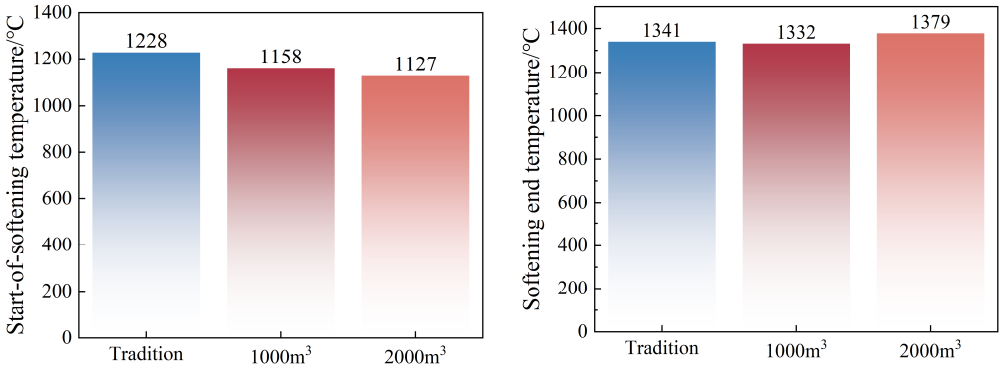
Figure 12. Microscopic morphology of pellets in different reduction stages.

3.4. Softening–Melting Behavior of Burden Under OBF Conditions

3.4.1. Softening Properties

Figure 13 shows the curve of the softening temperature of the charge. As the experimental conditions gradually increased from the traditional working conditions to the 1000 m^3 and 2000 m^3 working conditions, the initial softening temperature (T_{10}) and the final softening temperature (T_{40}) of the furnace charge did not show a single synchronous decreasing trend, but instead exhibited distinctly different evolutionary characteristics [30]. Among them, T_{10} exhibited a monotonically decreasing behavior, dropping from 1228 °C to 1127 °C. This is mainly because the increased residence time in the high reducing atmosphere greatly accelerates the stepwise reduction kinetics in the medium and low temperature range, causing high-valence iron oxides to rapidly transform into mesophase FeO within the furnace charge matrix before reaching the softening threshold. The local enrichment of FeO promotes its low-melting-point eutectic reaction with gangue minerals such as SiO_2, thereby causing the primary slag liquid phase to be generated and overflowed in advance [29]. However, as shown in Figure 13b, after a slight decrease

under the 1000 m^3 operating condition, T_{40} rebounded sharply under the 2000 m^3 blast furnace operating condition, rising back to 1374 °C. This anomalous increase is essentially controlled by a competitive mechanism between "liquid phase flow" and "solid structure support" [28]. Under 2000 m^3 conditions, the metallic iron in the outer layer of the furnace charge rapidly crystallizes, thickens, and undergoes intergranular nucleation and welding. This highly developed and continuous solid metallic iron rigid skeleton serves as a high-strength load-bearing skeleton, successfully encapsulating and constraining the initial slag liquid phase already generated inside the particles, greatly enhancing the bed's resistance to macroscopic deformation under high-temperature loads. This results in a delayed softening and collapse process of the furnace charge bed, pushing T_{40} to a higher temperature level and ultimately causing a significant widening of the overall softening range.



(**a**) Softening start temperature (**b**) Softening finishing temperature

Figure 13. The change curve of softening temperature of furnace charge.

3.4.2. Melting Properties

The melting start temperature (T_s) of the iron-bearing charge, which refers to that when the pressure of the material layer begins to rise sharply and indicates that the charge begins to enter the melt exudation stage under different conditions, are shown in Figure 14. At this time, the primary slag and the primary iron melt break through the metal iron shell and seep out, resulting in a sudden increase in the pressure difference of the material layer. Results show that T_s increased with the increasing oxygen enrichment; this is because the promotion in the reduction degree increases the thickness and strength of the metallic iron shell, enhances the constraint ability of the metallic iron shell to the melt, and increases the temperature required for the melt to break through, resulting in an increase in T_s.

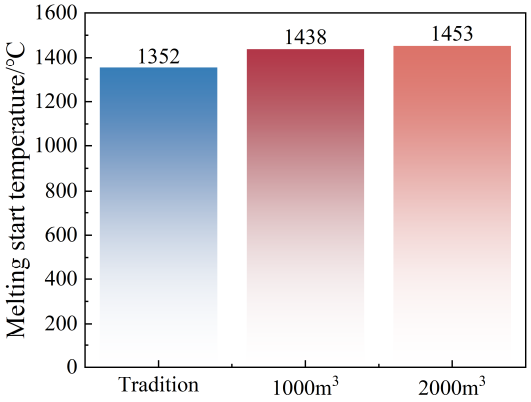


Figure 14. Melting start temperature.

Figure 15 shows the dripping temperature (T_d) of the charge. The variation in dripping temperature with the oxygen enrichment is small, indicating a limited influence of gas reduction potential on the dripping temperature of slag and iron.

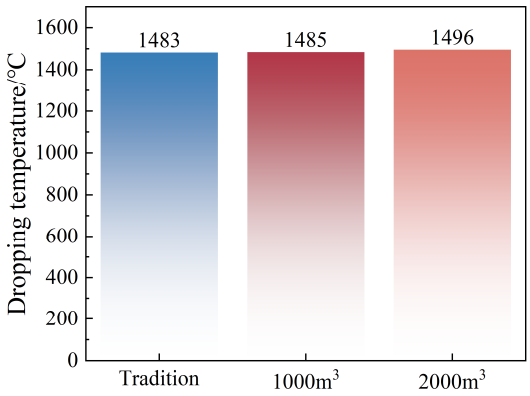


Figure 15. Dripping temperature.

3.4.3. Softening and Soft Melting Interval

Since the decrease in the softening start temperature of the charge is greater than that of the softening finishing temperature, with the increase in blast furnace volume, the softening interval (T_{40}–T_{10}) of the charge shows an overall expansion trend, and the position of the cohesive zone moves up in the blast furnace, as shown in Figure 16. The expansion of the cohesive zone means that the thickness of the material layer in the semi-molten state in the blast furnace increases, which puts forward higher requirements for the air flow distribution and permeability management in the furnace.

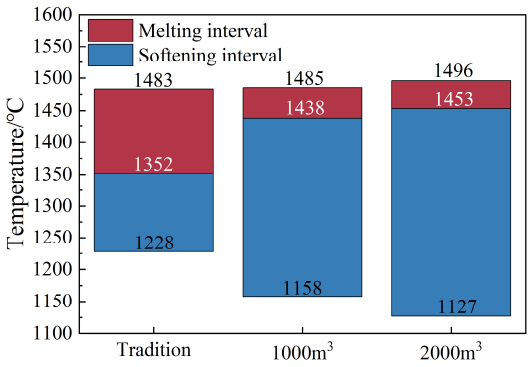


Figure 16. Softening and soft melting temperature range of charge.

3.4.4. Permeability of Gas and Liquid in Cohesive Zone

Figure 17 is the maximum pressure difference curve of iron-bearing charge. With the increase in oxygen enrichment, the maximum pressure difference (ΔP_{max}) of the cohesive zone gradually decreases, indicating that the gas permeability and liquid permeability of the cohesive zone are improved. The main reason is that with the increase in oxygen enrichment, the SiO_2 activity and basicity conditions of slag change accordingly, the viscosity of slag decreases and the fluidity increases, so the slag is more likely to flow out from the solid skeleton gap, thereby reducing the resistance of the material layer and improving the gas–liquid permeability of the cohesive zone. This result shows that under the premise of ensuring the reasonable burden structure, moderately increasing the degree of oxygen enrichment is conducive to improving the metallurgical properties of the cohesive zone in the blast furnace.

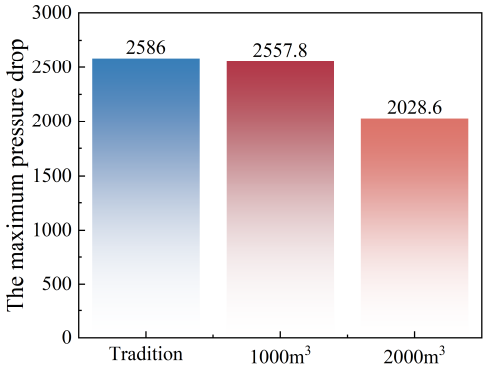


Figure 17. The pressure difference of the cohesive zone.

4. Conclusions

In this paper, the isothermal reduction kinetics, non-isothermal dynamic reduction behavior, and softening–melting characteristics of industrial sinter and pellets under simulated oxygen blast furnace (OBF) conditions were systematically investigated. The main conclusions are as follows:

(1) Isothermal reduction kinetics analysis confirms that gas–solid interfacial chemical reaction is the rate-controlling step for both sinter and pellets under OBF conditions. The apparent activation energies of sinter and pellets are 113.0 kJ·mol^{-1} and 57.9 kJ·mol^{-1}, respectively, revealing a substantial divergence driven by distinct microstructural constraints.

(2) Under the non-isothermal reduction conditions that reproduce the authentic spatial-temporal gradients of 1000 m^3 and 2000 m^3 OBFs, the high reduction potential of the gas atmosphere accelerates local FeO enrichment and its low-melting eutectic reaction with acid gangue minerals. This induces premature generation of fusible silicate primary slag, causing the softening start temperature T_{10} to decrease from 1228 °C to 1127 °C.

(3) Meanwhile, metallic iron rapidly precipitates and crystallizes on the burden surface under the strongly reducing atmosphere, forming an interconnected solid iron skeleton through high-temperature inter-particle welding. This in situ load-bearing framework encapsulates the internally molten primary slag and provides mechanical constraint that delays bed collapse. Under the 2000 m^3 condition, the softening end temperature T_{40} rebounds to 1374 °C and the melting start temperature T_s increases to 1453 °C.

(4) The synergistic interplay between early liquid formation and solid iron shell support effectively inhibits the premature clogging of inter-particle voids by high-viscosity FeO slag, thereby maintaining the gas–liquid permeability of the burden bed. This mechanism accounts for the 32.9% reduction in the maximum pressure drop ΔPmax of the cohesive zone under low-carbon OBF conditions, providing a scientific basis for burden optimization and gas permeability control in next-generation oxygen blast furnaces.

(5) This study shows that under OBF conditions, the burden resistance can be reduced by 32.9%, indicating that optimizing the burden structure helps improve the smooth operation of ultra-high oxygen-enriched blast furnaces and provides theoretical support for achieving a carbon emission reduction potential of 24–26%. For actual blast furnace operation, it is recommended to appropriately strengthen the central gas flow to alleviate the permeability pressure caused by the upward shift and thickening of the softening zone. Simultaneously, the burden structure should maintain a reasonable ratio of sinter to high-oxidation pellets, and the formation of a solid "rigid metallic iron skeleton" should be promoted by controlling the temperature gradient in the medium-

and high-temperature zones, thereby improving the stability and low-carbonization level of blast furnace operation under full oxygen injection conditions.

Author Contributions: Conceptualization, R.X. and J.Z.; methodology, Y.Z. and R.W.; writing—original draft preparation, Y.Z.; writing—review and editing, R.W. and J.Z.; visualization, Y.Y. and A.N.C.; supervision, J.S.; project administration, R.X.; funding acquisition, J.Z. All authors have read and agreed to the published version of the manuscript.

Funding: This research was funded by the National Natural Science Foundation of China (No. 52274316, U24A20102), National Key R&D Program of China (No. 2024YFE0208900, 2022YFE0208100).

Data Availability Statement: The original contributions presented in this study are included in the article. Further inquiries can be directed to the corresponding authors.

Conflicts of Interest: The authors declare no conflicts of interest.

References

1. Jiang, W.; Jung, T.; Dai, H.; Xiang, P.; Chen, S. Transition Pathways for Low-Carbon Steel Manufacture in East Asia: The Role of Renewable Energy and Technological Collaboration. *Sustainability* **2025**, *17*, 4280. [CrossRef]
2. Zhang, S.R.; Yu, Z.J. Development of Ironmaking Technology in the Past 60 Years. *Iron Steel* **2014**, *49*, 8–14.
3. IEA. *Iron and Steel Technology Roadmap*; International Energy Agency: Paris, France, 2020.
4. Li, J.; Xie, C.; Cai, J.; Wang, C. Low Carbon Development Pathway of China's Iron and Steel Industry under the Vision of Carbon Neutrality-Consensus and Uncertainty. *Chin. J. Environ. Manag.* **2022**, *14*, 48–53.
5. Nogami, H.; Kashiwaya, Y.; Yamada, D. Simulation of Blast Furnace Operation with Intensive Hydrogen Injection. *ISIJ Int.* **2012**, *52*, 1523–1527. [CrossRef]
6. Chu, M.; Nogami, H.; Yagi, J.I. Numerical Analysis on Injection of Hydrogen Bearing Materials into Blast Furnace. *ISIJ Int.* **2004**, *44*, 801–808. [CrossRef]
7. Vogl, V.; Åhman, M.; Nilsson, L.J. Assessment of hydrogen direct reduction for fossil-free steelmaking. *J. Clean. Prod.* **2018**, *203*, 736–745. [CrossRef]
8. Allanore, A.; Yin, L.; Sadoway, D.R. A New Anode Material for Oxygen Evolution in Molten Oxide Electrolysis. *Nature* **2013**, *497*, 353–356. [CrossRef] [PubMed]
9. Takahashi, K.; Nouchi, T.; Sato, M.; Ariyama, T. Perspective on Progressive Development of Oxygen Blast Furnace for Energy Saving. *ISIJ Int.* **2015**, *55*, 1866–1875. [CrossRef]
10. Fabian, R.; Dionissios, P.; Kriston, B.; Kelvin, Y.; Rajesh, A.; Tom, A.; Hanna, B. Green steel: Design and cost analysis of hydrogen-based direct iron reduction. *Energy Environ. Sci.* **2023**, *16*, 4121–4134. [CrossRef]
11. Cui, X.J.; Hu, C.Q. Research trends and prospects of hydrogen-rich ironmaking in blast furnace. *China Metall.* **2024**, *34*, 1–10.
12. Fan, Z.; Friedmann, S.J. Low-carbon production of iron and steel: Technology options, economic assessment, and policy. *Joule* **2021**, *5*, 829–862. [CrossRef]
13. Sohn, H.Y. Suspension ironmaking technology with greatly reduced energy requirement and CO2 emissions. *Steel Times Int.* **2007**, *78*, 354–362.
14. Liu, Y.; Wang, Z.; Wang, G.; Liu, L. Analysis of technological paths under the goal of green and low-carbon transformation in the steel industry of China. *J. Environ. Eng. Technol.* **2026**, *16*, 569–578.
15. Danloy, G.; Berthelemot, A.; Grant, M.; Borlée, J.; Sert, D.; Van der Stel, J.; Jak, H.; Dimastromatteo, V.; Hallin, M.; Eklund, N.; et al. ULCOS-pilot testing of the low-CO_2 blast furnace process at the experimental BF in Luleå. *ISIJ Int.* **2009**, *49*, 1461–1468.
16. Zhang, Z.D.; Tang, Y.; Chu, M.S. Comprehensive evaluation on low carbon iron making technology of top gas recycling oxygen blast furnace. *Iron Steel* **2023**, *58*, 81–91+126.
17. Meijer, K.; Zeilstra, C.; Teerhuis, C.; Ouwehand, M.; Van Der Stel, J. Developments in alternative ironmaking. *Trans. Indian Inst. Met.* **2013**, *66*, 475–481. [CrossRef]
18. Ding, Z.F.; Xing, X.D.; Zhe, Y.; Shen, Z.H.; Li, J.X.; Li, H.Z.; Lv, M. Research progress on high temperature interaction of blast furnace iron-bearing burden. *China Metall.* **2024**, *34*, 1–14. [CrossRef]
19. Hooey, P.L.; Bodén, A.; Wang, C.; Grip, C.-E.; Jansson, B. Design and application of a spreadsheet-based model of the blast furnace factory. *ISIJ Int.* **2010**, *50*, 924–930. [CrossRef]
20. Lan, C.C. Functional behavior of coke with different reactivity in reduction-softening-melting process of burden. *Iron Steel* **2023**, *58*, 18–25.
21. Nogami, H.; Yagi, J.I.; Kitamura, S.Y.; Austin, P.R. Analysis on Material and Energy Balances of Ironmaking Systems on Blast Furnace Operations with Metallic Charging, Top Gas Recycling and Natural Gas Injection. *ISIJ Int.* **2006**, *46*, 1759–1766. [CrossRef]

22. Heikkinen, E.P.; Fabritius, T. Modelling of the reduction kinetics of iron ore pellets in a blast furnace atmosphere. *J. Phys. Conf. Ser.* **2011**, *297*, 012031.
23. Heikkilä, A.; Iljana, M.; Bartusch, H.; Fabritius, T. Reduction of Iron Ore Pellets, Sinter, and Lump Ore under Simulated Blast Furnace Conditions. *Steel Res. Int.* **2020**, *91*, 2000047. [CrossRef]
24. Cao, Z.S.; Xu, Q.; Kang, H.P.; Lu, X.Y.; Shi, J.; Chen, B.; Guo, L.J. Non-isothermal reduction characteristics and kinetic analysis of hematite in hydrogen-rich atmosphere. *Chem. Ind. Eng. Prog.* **2026**, *45*, 1181–1189.
25. Lyu, Q.; Qie, Y.; Liu, X.; Lan, C.; Li, J.; Liu, S. Effect of hydrogen addition on reduction behavior of iron oxides in gas-injection blast furnace. *Thermochim. Acta* **2017**, *648*, 79–90. [CrossRef]
26. Hou, B.; Zhang, H.; Li, H.; Zhu, Q. Study on Kinetics of Iron Oxide Reduction by Hydrogen. *Chin. J. Chem. Eng.* **2012**, *20*, 10–17. [CrossRef]
27. Spreitzer, D.; Schenk, J. Reduction of iron oxides with hydrogen—A review. *Steel Res. Int.* **2019**, *90*, 1900108. [CrossRef]
28. Wang, Y.F.; Qie, Y.N.; Zhang, S.H.; Zhu, J.Q.; Liu, R.; Ji, H. Research status and prospect of softening-melting properties for blast furnace charge. *China Metall.* **2024**, *34*, 1–9+23.
29. Tan, P.L.; Zhang, J.L.; Huang, J.Q.; Wang, Y.Z.; Liu, Z.J.; Han, F.G. Effect of sinter basicity on the interactive reaction of composite burdens. *Chin. J. Eng.* **2023**, *45*, 890–898.
30. Zhang, H.J.; She, X.F.; Han, Y.H.; Wang, J.S.; Zeng, F.B.; Xue, Q.G. Softening and Melting Behavior of Ferrous Burden under Simulated Oxygen Blast Furnace Condition. *J. Iron Steel Res. Int.* **2015**, *22*, 297–303. [CrossRef]
31. *GB/T 6730.5-2022*; Iron Ores—Determination of Total Iron Content—Titrimetric Methods After Titanium(III) Chloride Reduction. Standards Press of China: Beijing, China, 2022.
32. *GB/T 6730.8-2016*; Iron Ores—Determination of Iron(II) Content—Potassium Dichromate Titrimetric Method. Standards Press of China: Beijing, China, 2016.
33. *GB/T 6730.62-2005*; Iron Ores-Determination of Calcium, Silicon, Manganese, Titanium, Phosphorus Magnesium, Aluminium and Barium Content Wavelength Dispersive X-Ray Fluorescence Spectrometric Method. Standards Press of China: Beijing, China, 2005.
34. *GB/T 13241-2017*; Iron Ores—Determination of Reducibility. Standards Press of China: Beijing, China, 2017.
35. Klimczyk, A.; Słowiński, K.; Karbowniczek, M. Calculation of coke layers situation in the cohesive zone of blast furnace. *Materials* **2021**, *14*, 192. [CrossRef]
36. Fu, D.; Chen, Y.; Zhou, C.Q. Mathematical modeling of blast furnace burden distribution with non-uniform descending speed. *Appl. Math. Model.* **2015**, *39*, 7554–7567. [CrossRef]
37. Yu, X.; Shen, Y. Computational fluid dynamics study of the thermochemical behaviors in an ironmaking blast furnace with oxygen enrichment operation. *Metall. Mater. Trans. B* **2020**, *51*, 1760–1772. [CrossRef]
38. Wei, R.F. Reaction behavior of burden above soft melting zone in carbon cycle oxygen blast furnace. *Iron Steel* **2023**, *58*, 69–81.
39. *GB/T 34211-2017*; Iron Ores—Method for Determination of Iron Reduction Softening Drippinger Performance Under Load. Standards Press of China: Beijing, China, 2017.

Disclaimer/Publisher's Note: The statements, opinions and data contained in all publications are solely those of the individual author(s) and contributor(s) and not of MDPI and/or the editor(s). MDPI and/or the editor(s) disclaim responsibility for any injury to people or property resulting from any ideas, methods, instructions or products referred to in the content.